 doi:10.20944/preprints202009.0397.v1

Article

Broadband time-resolved absorption and dispersion spectroscopy of methane and ethane in a plasma using a mid-infrared dual-comb spectrometer

Muhammad Ali Abbas*, Luuk van Dijk, Khalil Eslami Jahromi , Mohammadreza Nematollahi, Frans J.M. Harren and Amir Khodabakhsh

Trace Gas Research Group, Department of Molecular and Laser Physics, Institute of Molecules and Materials, Radboud University, 6525 AJ Nijmegen, The Netherlands; Luuk.vandijk@student.ru.nl (L.V.D.); Kh.Eslami@science.ru.nl (K.E.J.); M.Nematollahi@science.ru.nl (M.N.); F.Harren@science.ru.nl (F.J.M.H.); A.Khodabakhsh@science.ru.nl (A.K.)

* Correspondence: A.Abbas@science.ru.nl

Abstract: Conventional mechanical Fourier Transform Spectrometers (FTS) are able to simultaneously measure absorption and dispersion spectra of gas-phase samples. However, they usually need very long measurement times to achieve time-resolved spectra with a good spectral and temporal resolution. Here, we present a mid-infrared dual-comb-based FTS in an asymmetric configuration, providing broadband absorption and dispersion spectra with a spectral resolution of 5 GHz, a temporal resolution of 20 μs, and a total measurement time of a few minutes. We used the dual-comb spectrometer to monitor the reaction dynamics of methane and ethane in an electrical plasma discharge. We observed ethane/methane formation as a recombination reaction of hydrocarbon radicals in the discharge in various static and dynamic conditions. The results demonstrate a new analytical approach for measuring fast molecular absorption and dispersion changes and monitoring fast dynamics of chemical reactions, which can be interesting for chemical kinetic research and particularly for the combustion and plasma analysis community.

Keywords: Dual frequency comb spectroscopy; mid-infrared absorption and dispersion spectroscopy; electrical discharge plasma; time-resolved plasma kinetics

1. Introduction

The conversion of ethane and methane to other hydrocarbons in plasmas has been extensively studied, both theoretically and experimentally. Different non-thermal plasma techniques such as Direct Current (DC), microwave or RF discharge, dielectric barrier discharge (DBD), and corona or spark discharge have been demonstrated for this purpose under various conditions [1-8]. One of the primary goal of these studies is to develop an efficient method and process for converting small hydrocarbons like methane to other valuable hydrocarbons. It is particularly advantageous to find an efficient non-thermal (non-equilibrium) plasma operation for this purpose, since it requires less energy and operates at lower temperatures, compared to thermal (equilibrium) plasmas [9]. To characterize the plasma process and maximize the conversion efficiency, different molecular species and reaction processes should be measured and continuously monitored during the plasma operation. Different methods are employed for this purpose, which are mostly based on mass spectrometry [10] or various in-situ optical detection techniques, such as emission and absorption spectroscopy [11-15]. The main advantages of the optical-based diagnostics over the other methods are their fast response time, *in-situ* measurement, and species specificity. Among the many laser-based, gas spectroscopic methods, plasma diagnosis in the mid-infrared wavelength region of 2 -20 μm is of the great interest, since the strong fundamental ro-vibrational transitions of the majority of molecules lie there. This region is also called the "fingerprint" region, due to the unique spectral

Preprints (www.preprints.org) | NOT PEER-REVIEWED | Posted: 17 September 2020 doi:10.20944/preprints202009.0397.v1

features of the molecules. The coherent mid-infrared sources for probing these fundamental transitions can be either narrowband or broadband. Among the narrowband sources, tunable lead-salt diode lasers have been applied for plasma diagnosis, detecting mid-infrared active compounds like hydrocarbons, fluorocarbon, boron, etc. A comprehensive review can be found in [16] and references therein. The main disadvantage of using lead-salt lasers is their need for cryogenic cooling and narrowband tuning rang (~7 cm^{-1}) limiting the number of detectable species. Recent advances in the cw and pulsed quantum cascade lasers (QCL) and interband cascade lasers (ICL) led to the greater flexibility and compactness of the mid-infrared sources for plasma diagnostics. In continuous wave (cw) narrowband operation, these new sources can be tuned mechanically (in an external cavity configuration) in order to probe absorption transitions of multiple species in a broad optical bandwidth (~300 cm^{-1}). Alternatively, in pulsed broadband operation they can be used in combination with a Fourier Transform Spectrometer (FTS) [17] or a dispersive based spectrometer [18, 19] to simultaneously record broadband spectra. The use of these mid-infrared sources for plasma diagnostics is comprehensively discussed in [20, 21].

In the past decade, mid-infrared Dual-Comb Spectroscopy (DCS) [22-24] has emerged as an alternative technique to traditional FTS, providing sub-second sampling times. In DCS, the interferogram is made by the interference of femtosecond pulses from two mode-locked lasers, each generating a frequency comb, which have a slightly different repetition frequency with respect to each other. Similar to traditional FTS, the interferogram is recorded using a single-point detector and the absorption spectrum is achieved by a Fourier transformation of the recorded interferogram. Due to its inherent short measurement time, mid-infrared DCS have received increasing attention in various applications such as combustion diagnostics [25-27], study of protein dynamics [28], radical-radical interactions in flash photolysis mixtures [29], and DC/pulsed plasma discharges [30].

To measure dispersion spectra next to absorption spectra, dispersive FTS and DCS in an asymmetric arrangement have been demonstrated in various studies [31-38]. For this, the sample is placed in one arm of the interferometer, and an asymmetric interferogram is recorded on a single point detector, hence the name asymmetric/dispersive FTS. This technique can provide a full picture of molecular absorption and dispersion spectra, corresponding to the ro-vibrational transitions and yield the complex refractive index of the sample.

In this study, we have modified our DCS, to be able to measure simultaneously time-resolved absorption and dispersion spectra. We present broadband mid-infrared absorbance/dispersion spectra of methane and ethane under static and dynamic conditions, induced by a DC discharge. Spectra are measured with a spectral resolution of 5 GHz, with a spectral bandwidth of 2850-3150 cm^{-1} and a time resolution of 20 μs. Simultaneous monitoring of the phase and absorbance variations in plasma processes are particularly useful to measure the complex susceptibility and refractive index of materials involved in the plasma, which is an indication of the plasma density [39]. To the best of our knowledge, this is the first demonstration of broadband time-resolved absorption/dispersion spectroscopy in the mid-infrared wavelength range for plasma diagnostics.

2. Materials and Methods

2.1. Absorption and Dispersion Spectroscopy

A monochromatic electromagnetic (light) wave probing a gas sample, experiences a change in phase and amplitude at a frequency which is in resonance with a molecular transition, is given as

$$\boldsymbol{E = E_0 e^{i(\omega t - k_0 n_a l)}}, \quad (1)$$

where E_0 is the amplitude of the electric field, ω is the angular frequency of the light, k_0 is the wave vector pointing in propagation direction, l is the interaction length of light with the sample and n_a is the complex refractive index of the sample near a molecular transition, which is generally a function of the frequency of light, $\nu = \omega/2\pi$. At a particular time instant $(t = 0)$

$$\boldsymbol{E = E_0 e^{i(-k_0 n_a l)}}, \quad (2)$$

Preprints (www.preprints.org) | NOT PEER-REVIEWED | Posted: 17 September 2020 doi:10.20944/preprints202009.0397.v1

and near the molecular resonance, complex refractive index is given as [40]

$$\boldsymbol{n_a(v) = n + n'(v) - i\kappa(v)}, \quad (3)$$

in which n is the non-resonant refractive index and $n'(v) - i\kappa(v)$ is the complex resonant component, where $n'(v)$ represents the dispersion and $\kappa(v)$ is the extinction coefficient, the latter describing the absorption of the light wave appearing in Lambert-beer law as $I = I_0 e^{-(2k_0\kappa(v)l)}$.

Phase change in radians, $\Delta\varphi$, experienced by the light in the medium, is proportional to the dispersion $n'(v)$ and is given by

$$\boldsymbol{\Delta\varphi = 2k_0 n'(v) l}, \quad (4)$$

and the absorbance of light is given by:

$$\boldsymbol{\alpha l = 2k_0 \kappa(v) l}. \quad (5)$$

Dispersion spectroscopy has two main advantages: (i) dispersion spectra are always proportional to the concentration of the gas species, whereas absorption spectra saturate for high concentrations. Therefore, phase spectroscopy provides a larger dynamic range to measure highly absorbing samples. (ii) dispersion spectra can be immune to intensity fluctuations, as the phase is only dependent on the refractive index and not on the laser intensity [41]. Most spectroscopic methods, which simultaneously record molecular absorption and dispersion, are based on tunable cw lasers [40], using Frequency Modulation Spectroscopy (FMS) [42], Noise-Immune Cavity-Enhanced Optical Heterodyne Molecular Spectroscopy (NICE-OHMS) [43, 44], Heterodyne Phase Sensitive Dispersion Spectroscopy (HSPDS) [45], Chirped Laser Dispersion Spectroscopy (CLaDS), [46] or Faraday Rotation Spectroscopy (FRS) [47]. FTS [48] and Vernier spectroscopy [49] are two broadband methods, which are able to extract absorbance and phase changes of samples, simultaneously. Two common FTS methods for this purpose are Dispersive Fourier Transform Spectroscopy (DFTS) [31] and Dual Comb Spectroscopy (DCS) [33, 36]. In DFTS, the sample is placed in one arm of the Michelson interferometer and a single-sided asymmetric interferogram is obtained on the detector in the time domain by scanning the retro-reflecting mirror in the FTS. This asymmetric shape of the interferogram indicates that both absorption and dispersion can be obtained after applying a fast Fourier transform (FFT). Similarly, in DCS this information can be obtained by placing the sample in the path of one of the frequency comb beams, while the other comb beam bypasses the sample before being combined with the first comb beam. As mentioned earlier, the main advantage of DCS compared to a mechanical FTS is the lack of moving mirrors, which yields a very fast data acquisition with high spectral and temporal resolution.

2.2. Experimental Setup

Figure 1 demonstrates the schematic of the experimental setup. It consists of the mid-infrared dual-comb source, the DCS and the plasma discharge system. Here, we explain each sub-system, as well as the data acquisition and signal processing in the following subsections.

Preprints (www.preprints.org) | NOT PEER-REVIEWED | Posted: 17 September 2020 doi:10.20944/preprints202009.0397.v1

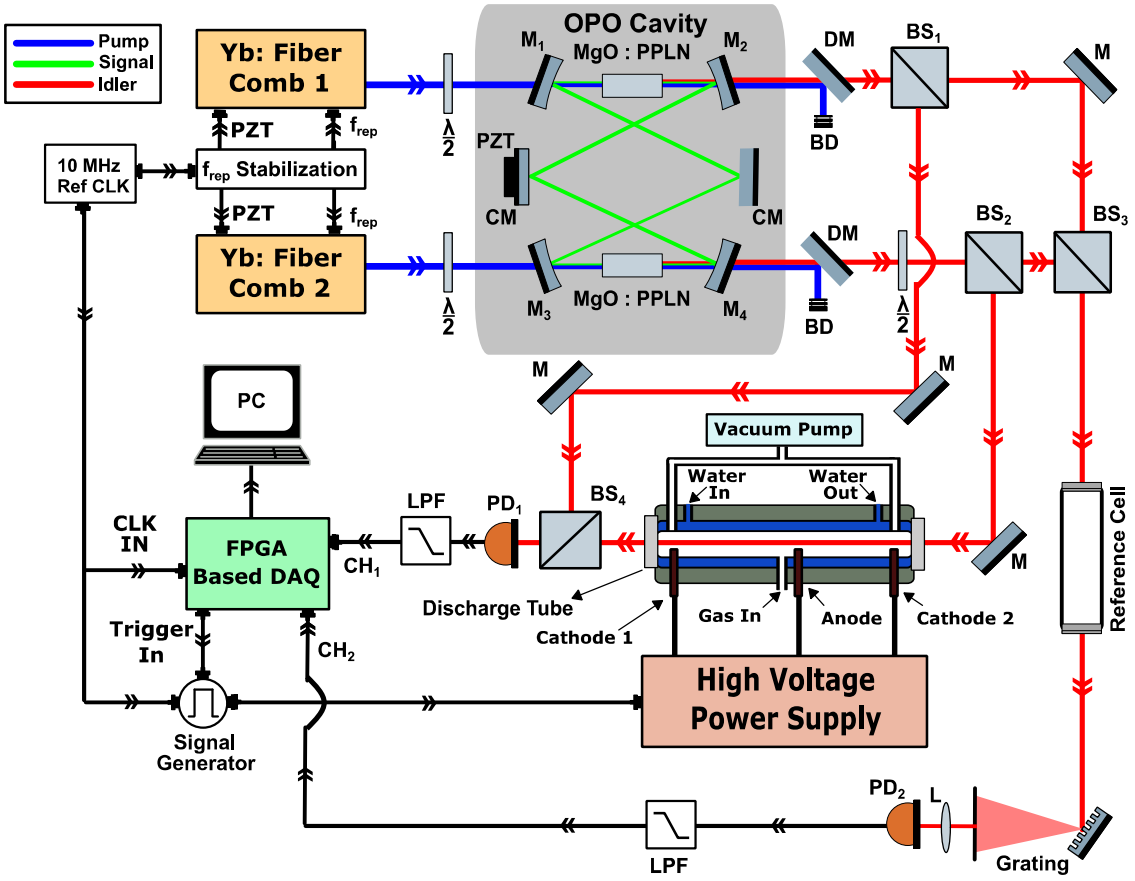

Figure 1. Experimental setup for mid-infrared dual-comb absorption and dispersion spectroscopy in an electrical discharge plasma. M_{1-4}, curved cylindrical mirrors; CM, chirped mirrors; PZT, piezoelectric transducer; BS_1 and BS_2, pellicle beam splitter for beam division; BS_3 and BS_4, pellicle beam splitters for beam combination; BD, beam dumps; $PD_{1,2}$, HgCdTe photodetectors.

2.2.1. Mid-Infrared Dual-Comb Source

Two near-infrared, Yb-fiber-based, femtosecond mode-locked lasers (1064 nm, Menlo Systems, Germany), with stabilized repetition frequency (f_{rep}, 90 MHz) and free running carrier-envelope offset frequencies (f_{ceo}), were used as pump sources for two singly-resonant, optical parametric oscillators (OPOs) sharing a single ring cavity [33]. For DCS, one pump comb had a slightly different repetition frequency (f_{rep}) with respect to the second comb, so that the difference in the repetition frequency (Δf_{rep}) could be set between 200 to 300 Hz. A 10 MHz reference clock was used for referencing all of the frequency sources used in f_{rep} control electronics, triggering of the data acquisition, and modulating the discharge [30, 50].

The two mode locked laser beams were set to be orthogonally polarized, using half-wave plates before entering the OPO in a counter-propagating manner. Two 5-mm-long periodically poled Lithium Niobate (PPLN) crystals (Covesion Ltd., UK.), containing 8 poling periods, were used in the OPO. The OPO has a ring cavity configuration and consists of four concave mirrors (AR coated at 1064, and 3650-4850 nm, HR coated at 1350-1500 nm, Layertec GmbH, Germany) with focal length of 5 cm, and six flat chirp mirrors (HR coated 1370-1750 nm,) for dispersion compensation (for simplicity Figure 1 shows two chirp mirrors). One of the chirped mirrors was mounted on a translational stage, connected to a piezo- electronic transducer (PZT) for coarse and fine-tuning of the length of the OPO cavity. The cavity length was adjusted around 330 cm, to match the repetition frequencies (f_{rep}) of both near-infrared pump lasers (~90 MHz), enabling both of the counter propagating signal beams to be in resonance with the cavity modes [33]. Two orthogonally polarized mid-infrared beams were generated from the OPO, with a spectral bandwidth (full width half maximum) of ~300 cm^{-1} and 200

Preprints (www.preprints.org) | NOT PEER-REVIEWED | Posted: 17 September 2020 doi:10.20944/preprints202009.0397.v1

mW of maximum average power. A half-wave plate was used for rotating the polarization of one mid-infrared beam to align both polarizations.

2.2.2. Dual-Comb Spectrometer Design for Absorption/Dispersion Spectroscopy

As shown in Figure 1, each beam was split into two channels, called the sample and reference channels. In the sample channel, a 50-cm-long discharge tube is placed, whereas in the reference channel a 30-cm-long absorption cell is placed for optical frequency calibration. For the splitting of each beam, we used two 50:50 beam splitters (BS_1 and BS_2) and for combining also two 50:50 beam splitters (BS_3 and BS_4). In the sample channel, the idler beam of comb-2 passes through the discharge tube, while the idler beam of comb-1 bypasses the tube, and the two beams are combined on BS_4. In the reference channel, the two idler beams are combined by BS_3 and afterward both pass through the reference gas cell (containing pure methane at 100 mbar). Therefore, the sample channel has an asymmetric configuration (providing both absorption and dispersion spectra), while the reference channel is symmetric (only yielding the absorption spectra). The asymmetric interferogram of the sample channel is detected by an HgCdTe photodetector (PD_1, 50 MHz bandwidth, PVI-4TE Vigo, Poland), as shown in Figure A1 in the appendix (in blue). The reference absorption cell is used for absolute frequency calibration of the sample spectrum. The output beam from the reference cell is dispersed with the help of a diffraction grating, and a mechanical slit is used to band-pass filter the spectrum around a single line of methane centered at 3038.5 cm^{-1}, before focusing the beam on a HgCdTe photodetector, (PD_2, 50 MHz bandwidth, PVI-4TE Vigo, Poland). We use the optical frequency position of this reference absorption line for removing the f_{ceo} fluctuations and frequency calibration of the dual-comb spectrum. More details on absolute frequency calibration can be found in [50].

As the femtosecond pulses need to arrive at the same time on the detectors, the lengths of sample and reference channels were adjusted in such a way that both idler combs travel an equidistant path from the generation point in the non-linear crystal to the recombination beam splitters, i.e. BS_3 and BS_4. This way we avoided any relative time-delay between sample and reference interferograms, and record both in the same time-frame of the data acquisition. Figure A1 (b) and (c) in the appendix show the effect of an induced displacement in time domain between the sample and reference interferograms, if a 3 mm thick CaF_2 window is inserted in the path of one of the beams. It clearly shows the sensitivity of the optical layout to a path length difference in any of these beams. Therefore, well-matched optical paths are necessary in this approach; however, no active control of the paths is required.

2.2.3. Discharge System and Gas Mixtures

As shown in Figure 1, the experimental setup for creating the discharge in static DC and dynamic operation, consists of a discharge tube, a high voltage power supply (Haefely Hipotronics, US) and an external signal generator (33500B, Agilent, US) for modulating the current of the HV power supply. The glass discharge tube is 50 cm long with 3 mm internal diameter. Water (at 23 °C) is flowing around the discharge tube at a constant flow rate to control the temperature of the discharge tube during operation. The discharge is split at the anode (in the center) to two hollow cathodes at the both ends of the tube. The anode is connected to the high voltage (HV) power supply with a maximum DC voltage of 25 kV and a maximum current of 40 mA. Each cathode is connected in series with a current regulator (containing ballast resistors) for limiting the current within acceptable bounds through the discharge tube.

In the discharge, we used two different gas mixtures of methane (40 %) in helium, and ethane (33 %) in helium, and studied the dynamics of absorption and dispersion spectra of the reactants and produced species in the discharge. For the methane-helium mixture experiment, a constant flow rate of 1.5 Nl/h (Normal Liters/hour) was applied using flow controllers, while for ethane a flow rate of 3 Nl/h was used. In both cases, a total pressure of 25-30 mbar was maintained in the discharge, using a pressure controller and a vacuum pump after the discharge tube. The inlet of the gas mixtures was chosen to be near the anode whereas the outlets are placed near the cathodes at the both ends, as

Preprints (www.preprints.org) | NOT PEER-REVIEWED | Posted: 17 September 2020 doi:10.20944/preprints202009.0397.v1

shown in Figure 1. This arrangement ensures that the molecular ions which are produced during the discharge operation and travel towards the two cathodes, do not oppose the gas follow direction. A static discharge operation was obtained by keeping the voltage and current at constant levels, while for dynamic discharge operation the discharge current was modulated by a square wave (on-off). A dual channel signal generator (33500B, Agilent), referenced to the same 10 MHz reference clock used for stabilizing the repetition rate of the two frequency combs, was employed to generate the square-wave modulation (at 265 Hz, 10% duty cycle). The second output of the signal generator was connected to the external trigger input of the data acquisition card to provide synchronization of the data acquisition and discharge pulses, as described in the next section.

2.2.4. Data Acquisition and Synchronization

Data acquisition of the spectrometer was controlled by a LabVIEW-based program. The hardware for fast data acquisition consists of a two channel AD convertor (NI-5762, National Instruments, US) in combination with a Field Programmable Gate Array module (FPGA, PXIe-7962R National Instruments, US). The interferograms from the sample and reference photodetectors are low pass filtered (at 50 MHz) and sampled with a rate of 125 MSample/s, recording 30,000 data points on each channel, yielding a single-shot acquisition time of $T_{acq} = 240$ µs. The recorded interferograms are stored in first-in-first-out (FIFO) buffers in the FPGA and transferred to the host PC, immediately after recording each sample and reference interferograms. Further data processing is performed offline using a MATLAB-based program. For microsecond time-resolved measurements, the dual channel signal generator (synchronized to the reference clock) is used to modulate the discharge by its first output channel and provides a trigger signal for the DAQ card on its second output channel. The second output channel of the signal generator can be manually delayed compared to the first one, providing a tunable time-delay between the discharge modulation and the triggering of the data acquisition. Therefore, transient discharge dynamics can be probed at different relative time-delays with respect to the discharge modulation. We used a minimum time-delay step of 20 µs to record the interferograms. The time-delay was fixed during a data acquisition time of ~3 seconds (used for averaging the spectra in the data processing routine) for each time-step, such that the entire period of the discharge modulation was probed at different intervals by a step-scanned mechanism. A more detailed description on timing schemes and synchronization can be found in [30].

2.2.5. Data Processing

The recorded interferograms are time stamped and post-processed using a Matlab-based program. In order to improve the signal-to-noise ratio and remove the ringing effect around the narrow absorption lines in the sample and reference spectra, a Blackman apodization function is applied to the interferograms in the post processing routine [50]. Afterward, a Fast Fourier Transform (FFT) is applied to each individual reference and sample interferogram yielding the reference and sample spectra in the RF domain. The spectra are then converted to the optical domain via the corresponding scaling factor ($f_{rep}/\Delta f_{rep}$). A shot-to-shot variable frequency shift remains in the measured spectra due to the f_{ceo} fluctuations on both mid-infrared combs. To remove these shifts, we use the known position of an absorption line in the reference spectrum (~3038.5 cm^{-1}) and correct for the shifts in both dispersion and absorption spectra of the sample. The absorption and dispersion spectra are averaged after the shift correction, yielding high SNR and absolute-frequency-calibrated spectra [50].

3. Results and Discussion

3.1. Proof of Principle

We evaluated the performance of the experimental set-up by measuring absorption and dispersion spectrum of methane diluted in helium (10% CH_4) at 30 mbar. Figure 2(a) shows the measured absorbance spectrum (in black, average of 700 shots, each single shot 240 µs acquisition

Preprints (www.preprints.org) | NOT PEER-REVIEWED | Posted: 17 September 2020 doi:10.20944/preprints202009.0397.v1

time), as well as the simulated methane absorbance spectrum (in red, inverted for clarity). The model spectrum is calculated from the HITRAN database, using a Voigt profile and convolving a Blackman instrument line-shape function corresponding to the applied apodization function to the interferogram, yielding a spectral resolution of 5 GHz. The measured and model spectra are in good agreement with each other. Figure 2(b) shows the measured phase (dispersion) spectrum of the gas sample retrieved from the same data set as the absorbance spectrum. The resonance dispersion features corresponding to the absorption peaks of methane are easily recognizable. The recorded phase and absorbance are direct measure of the molecular dispersion $n'(v)$ and complex extinction coefficient $\kappa(v)$, which are shown in Figure 2 (c) and 2(d) respectively.

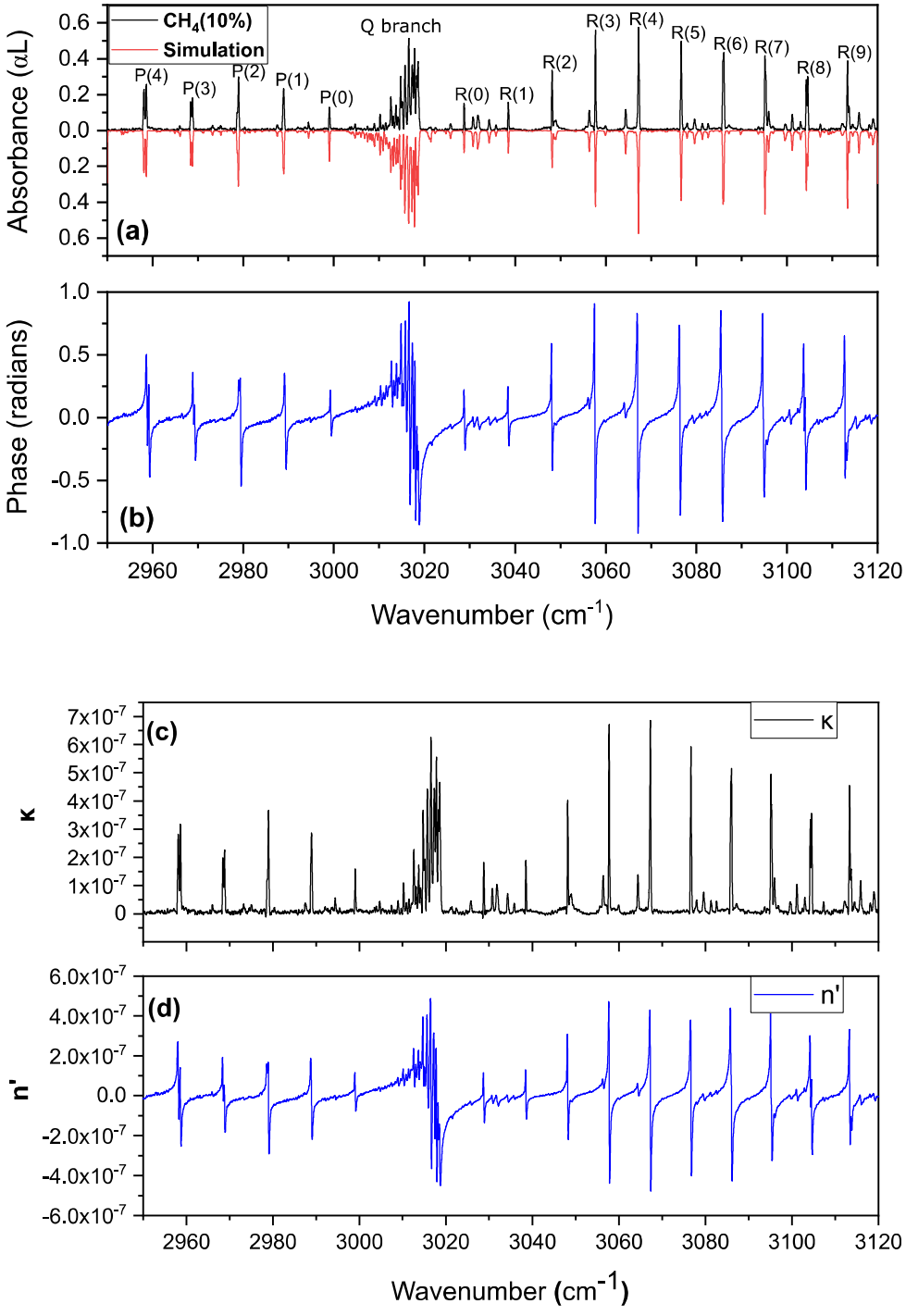

Preprints (www.preprints.org) | NOT PEER-REVIEWED | Posted: 17 September 2020 doi:10.20944/preprints202009.0397.v1

Figure 2. (a) Absorbance spectrum of 10% CH_4 diluted in He at 30 mbar (in black), along with a theoretical model spectrum of CH_4 (in red, inverted for clarity) using HITRAN database parameters. **(b)** Measured phase spectrum of 10% CH_4 diluted in He at 30 mbar. **(c)** Calculated extinction coefficient from the measured absorbance using equation (5). **(d)** calculated dispersion from the measured data of phase using equation (4).

The measured absorbance shown in Figure 2(a) can also be used to calculate the absorption cross-section (σ_v in m^2/molecule) of methane in a gas sample using:

$$\textbf{Absorbance} = \boldsymbol{\alpha l} = \boldsymbol{\sigma_v n l} \tag{6}$$

in which $\boldsymbol{n}$ is the particle density of the absorbent gas in molecules/m^3, given as:

$$\boldsymbol{n} = {}^{\boldsymbol{P}}/_{\boldsymbol{k_B T}} \tag{7}$$

in which $\boldsymbol{P}$ is the pressure, k_B is the Boltzmann constant and, $\boldsymbol{T}$ is the thermodynamic temperature. Hence, absorption cross-section is:

$$\boldsymbol{\sigma_v}(\textbf{cm}^2/\textbf{molecule}) = {}^{(\boldsymbol{10^4 \alpha k_B T})}/_{\boldsymbol{P}} \tag{8}$$

Instead of calculating σ_v for all possible frequencies in the ν_3 absorption band of methane, Figure 3, shows the specific absorption cross section of one branch line (P(1)) of methane. As the data of absorption cross-section are derived from the absorbance data in Figure 2(a), it automatically takes into account the broadening processes in terms of Voigt profile, convolved with Blackman instrumental line shape function.

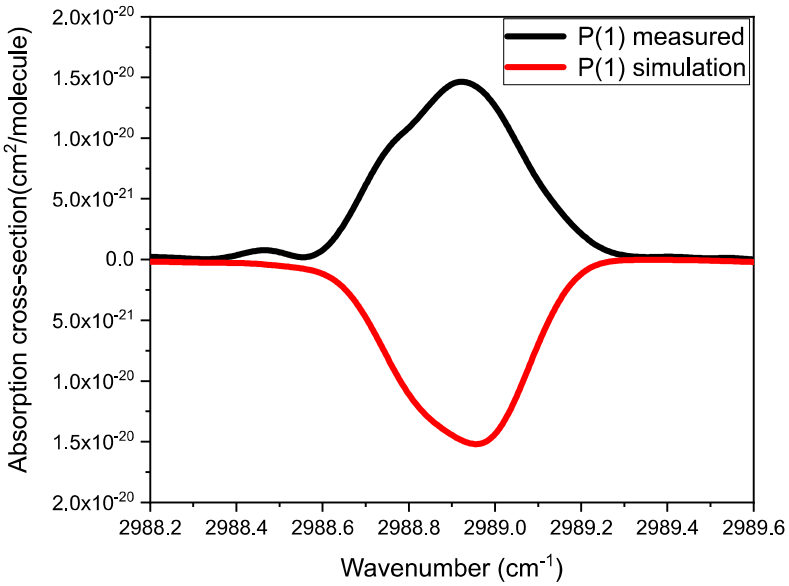

Figure 3. Measured (in black) and simulated (in red, Hitran database) absorption cross-section of P(1) branch line of methane ν_3 band, calculated for pressure of 30 mbar (3000 pascal) and temperature of 296 K.

3.2. Methane in a Static (DC) Discharge

In this section, we study the absorption and dispersion spectrum of methane (40% CH_4 in He, at 25 mbar) in a static discharge at a constant gas flow of 1.5 Nl/h. The absorption spectrum of the methane mixture before applying the discharge was measured first, as demonstrated in Figure 4 (a) (in blue, 600 averages). Thereafter, we applied a discharge with a stabilized current of 10 mA (DC voltage 10 kV), which corresponds to the current density of 1.41 mA/mm^2 passing through the discharge tube. The corresponding absorption spectrum of the methane mixture is illustrated in Figure 4 (a) (in red, 600 averages, inverted for clarity). It can be clearly seen that during the discharge

Preprints (www.preprints.org) | NOT PEER-REVIEWED | Posted: 17 September 2020 doi:10.20944/preprints202009.0397.v1

the intensity of methane absorption features decreases, which is an indication of reduced population of the methane molecules in the ground state and/or reduction in methane concentration. These are due to the vibrational/electronic excitation of methane molecules, as well as their fragmentation by electron impact into ions and neutral radicals. In other words, the reduction of methane (in the ground state) corresponds to a lower intensity of the absorbance (αl) features as shown in Figure 4 (a) (in the red spectrum), since absorbance is proportional to the concentration. At the same time, appearance of additional absorption features indicated by "*" is observed in the spectrum (in red). These absorption features correspond to strongest $^{R}Q_{K}$ lines from the ν_7 band of ethane (C_2H_6), along with more weaker lines, which corresponds to the P and R branch of the ν_7- band and ν_{10}-band of ethane in this spectral region [51, 52]. The HITRAN database only provides nine $^{R}Q_{K}$ lines for ethane in this spectral region, which are indicated by "*" and the two weaker lines are indicated by arrows in Figure 4 (a). As we are using a narrow discharge tube with an effective cooling capacity of water, the temperature of the gas mixture (296.15 K) does not vary before and during the discharge. As a result, we do not observe any change in the rotational distribution of the vibrational bands of methane and ethane, in Figure 4(a).

Ethane, which is produced in the discharge, is a result of recombination reaction of the radicals. However, it should be noted that electric discharge processes are very complex and contain numerous charged (ions), neutral species (atoms, radicals, excited molecules) and their interactions. Here, we restrict our discussion to excitation and de-excitation of the observed molecules, dissociation reaction by electron impact and consequent recombination of radicals to form new products. The main pathway to form C_2H_6, is the dissociation of CH_4 by an electron impact followed by recombination of two CH_3 radicals given as,

$$\mathbf{e} + \mathbf{CH_4} \rightarrow [\cdot\,\mathbf{CH_3}] + [\cdot\,\mathbf{H}] + \mathbf{e} \qquad \textbf{(dissociation)} \tag{9}$$

$$[\cdot\,\mathbf{CH_3}] + [\cdot\,\mathbf{CH_3}] \rightarrow \mathbf{C_2H_6} \qquad \textbf{(recombination)} \tag{10}$$

A more thorough analysis requires a detailed study on different dissociation and recombination reactions, their rate constants and conversion efficiencies of the species involved in the reaction, which is outside the scope of this work. It can be found elsewhere with various discharge conditions [53, 54].

The processes in the discharge also cause changes in refractive index of the gas media. Figure 4(b) shows the phase spectra of the gas sample before (in blue, 600 averages) and during the discharge (in red, 600 averages). Similar to the absorbance spectra, a decrease in the CH_4 phase spectral features as well as appearance of phase spectral features at optical frequencies corresponding to C_2H_6 ro-vibrational transitions after applying the discharge is clearly observed.

Preprints (www.preprints.org) | NOT PEER-REVIEWED | Posted: 17 September 2020 doi:10.20944/preprints202009.0397.v1

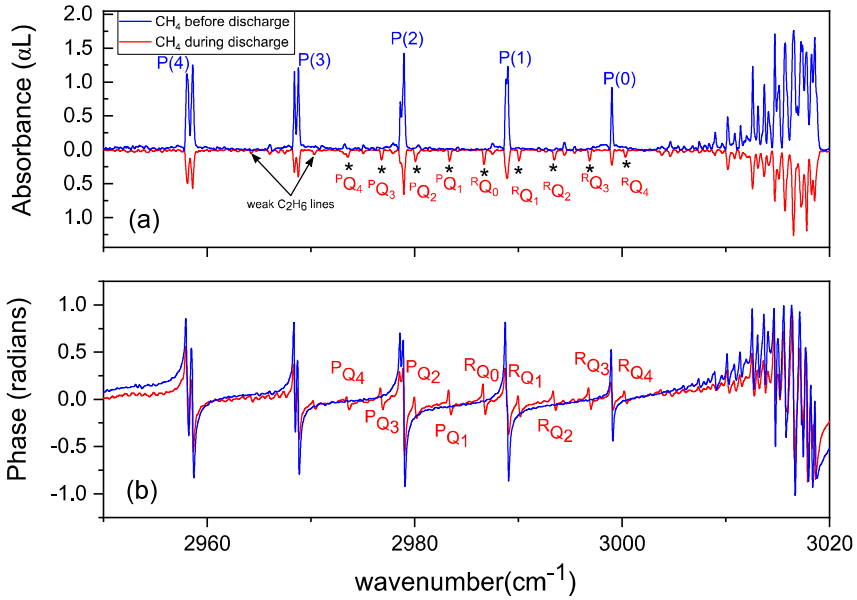

Figure 4. (a) Absorption spectra of 40% CH_4 diluted in He, at 25 mbar before (in blue, 600 averages) and during (in red, 600 averages, inverted for clarity) the discharge. **(b)** Corresponding dispersion spectra of the absorption spectra shown in **(a).**

To observe dissociation of methane and formation of ethane during a DC static discharge plasma with different current densities, we increased the current density of the discharge from 0 mA/mm^2 (no discharge) to 3.54 mA/mm^2, using a discharge voltage of ~10 kV. Note that the flow rate of the CH_4/He mixture was maintained at 1.5 Nl/h before and during the discharge. We introduced a waiting time of one minute prior to recording various spectra at different current values, to avoid transient states.

As we are only interested in the trends of methane and ethane during the discharge, we show the measured absorbance spectra for only a small wavenumber range (from 2980 to 3000 cm^{-1}) in Figure 5. Figure 5(a) and 5(b) show the measured absorbance spectra for different discharge current densities, demonstrating CH_4 and C_2H_6 absorption features. The consecutive absorbance spectra are shifted by an offset in order to get a good visual representation of the different absorbance intensities of both molecules. From discharge current density of 0 mA/mm^2 to 0.99 mA/mm^2, a clear decrease in the CH_4 absorption features can be observed. At the same time, C_2H_6 starts to form and thus its absorption features in the spectra are increasing. Similarly, from 1.27 to 3.54 mA/mm^2, continuous decrease in CH_4 absorption features can be seen, clearly indicating more depopulation from the vibrational ground state. However, C_2H_6 formation demonstrates a decrease at higher current densities, before settling to a semi-stable value. This decrease in C_2H_6 indicates that ethane molecules are exited and/or dissociated more, as enough energy is available for the produced ethane to react to new products. This described dynamics are shown in Figure 6, where the peak intensities of two different methane (P(1) and P(2)) and ethane ($^RQ_0$ and $^PQ_1$) absorption features, are plotted in terms of the discharge current density to provide a more clear representation of the dynamics of both molecules.

The same described dynamics of methane and ethane can be found in the phase spectra. Figure 7 shows the phase spectra for a single specific methane (P(1))and ethane ($^RQ_0$) absorption feature in terms of different discharge current densities. For methane and ethane, the phase spectral features show the same behavior as in the absorption spectra in Figure 5.

Preprints (www.preprints.org) | NOT PEER-REVIEWED | Posted: 17 September 2020 doi:10.20944/preprints202009.0397.v1

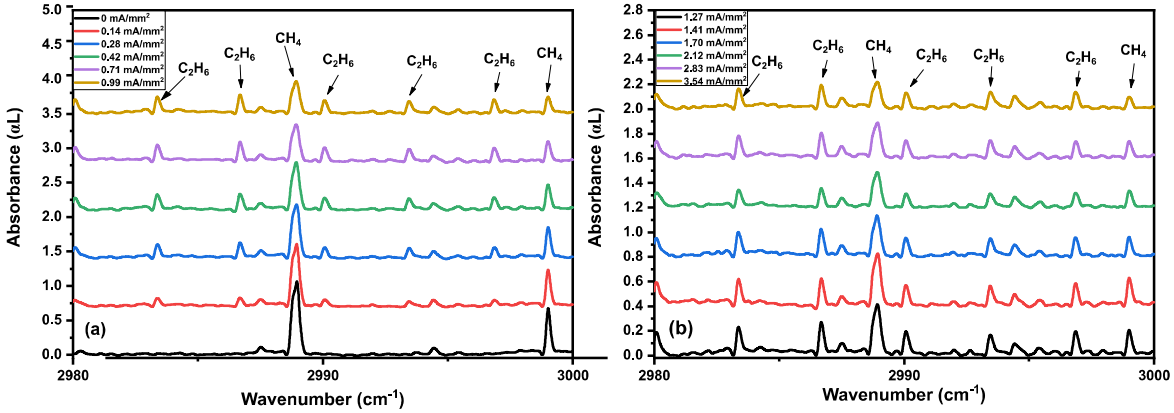

Figure 5. Absorption spectra of 40% CH_4 diluted in He, at 25 mbar at **(a)** 0 mA/mm² to 0.99 mA/mm² and **(b)** 1.27 mA/mm² to 3.54 mA/mm² discharge current densities, demonstrating the dynamics of methane and ethane absorption features. Consecutive spectra are vertically shifted for clarity.

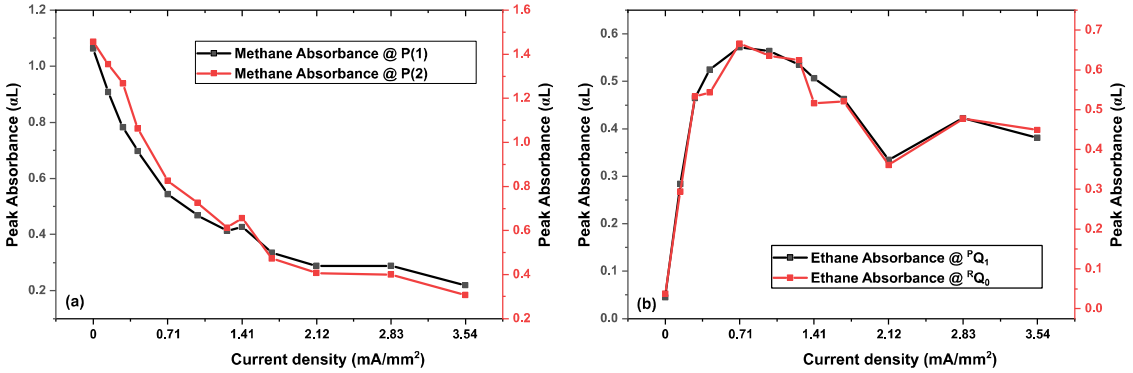

Figure 6. (a) Dynamics of methane peak absorbance in a 40% CH_4 diluted in He gas sample at 25 mbar upon increasing discharge current density. **(b)** Dynamics of ethane peak absorbance in the same sample. The peaks of two absorption features are plotted for each molecule to show the consistency of the dynamics.

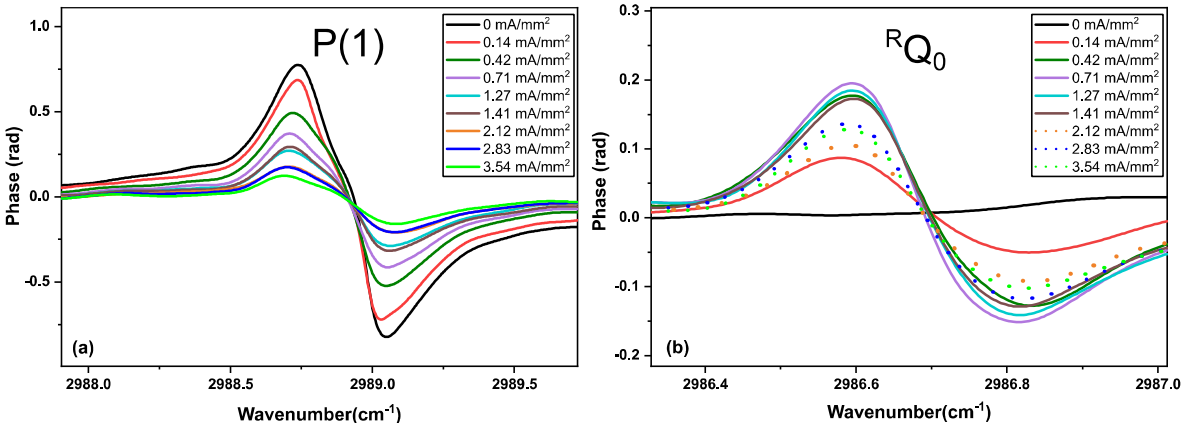

Figure 7. Dispersion (phase) spectra of **(a)** a methane absorption line of the gas sample (40% CH_4 diluted in He at 25 mbar) and **(b)** an ethane absorption line (produced by the discharge) upon increasing the discharge current density.

3.3. Ethane in a Static Discharge

In this section we study the absorption and dispersion spectra of ethane (33% diluted in helium, flow rate of 3 Nl/h, 25 mbar) before and during a static discharge with a stabilized current density of 0.71 mA/mm² (DC voltage ~10 kV). The absorbance spectrum before discharge is shown in Figure 8 (in black, 700 averages), and during the discharge in red (700 averages, inverted for clarity). Similar

Preprints (www.preprints.org) | NOT PEER-REVIEWED | Posted: 17 September 2020 doi:10.20944/preprints202009.0397.v1

to methane two different processes can be observed after applying the discharge. The intensity of the absorption features of ethane reduces indicating vibrational excitation/dissociation of ethane. Next to this, new absorption features appear in the spectrum although the ethane spectrum is very dense. Some of the new absorption features are clearly seen in the wavenumber region of 3050-3150 cm^{-1} and correspond to methane absorption lines; these were identified using the HITRAN database [55]. Two of these features are indicated with arrows in Figure 8.

Methane production in an ethane mixture discharge can be explained as a three-stage reaction. Firstly, the cleavage of the C-C bond of C_2H_6 by an electron impact into two CH_3 radicals (equation 11). Secondly, the cleavage of the C-H bond of C_2H_6 by an electron impact into C_2H_5 and H radicals (equation 12), and finally recombination of CH_3 and H radicals to form CH_4 (equation 13). Note that, this is only one of the pathways of reaction to obtain methane from an ethane discharge, as described in [53],

$$\mathbf{e} + \mathbf{C_2H_6} \rightarrow [.\mathbf{CH_3}] + [.\mathbf{CH_3}] + \mathbf{e} \qquad \textbf{(dissociation)} \tag{11}$$

$$\mathbf{e} + \mathbf{C_2H_6} \rightarrow [.\mathbf{C_2H_5}] + [.\mathbf{H}] + \mathbf{e} \qquad \textbf{(dissociation)} \tag{12}$$

$$[.\mathbf{CH_3}] + [.\mathbf{H}] \rightarrow \mathbf{CH_4} \qquad \textbf{(recombination)} \tag{13}$$

The production of methane can also been observed in the phase spectra, as depicted in Figure 9 for the wavenumber span of 3070-3145 cm^{-1}. The resonance phase features corresponding to methane transitions are indicated by "*". The high SNR phase spectrum helps to distinguish weak features from the noise, which are usually harder to distinguish in the absorption spectrum.

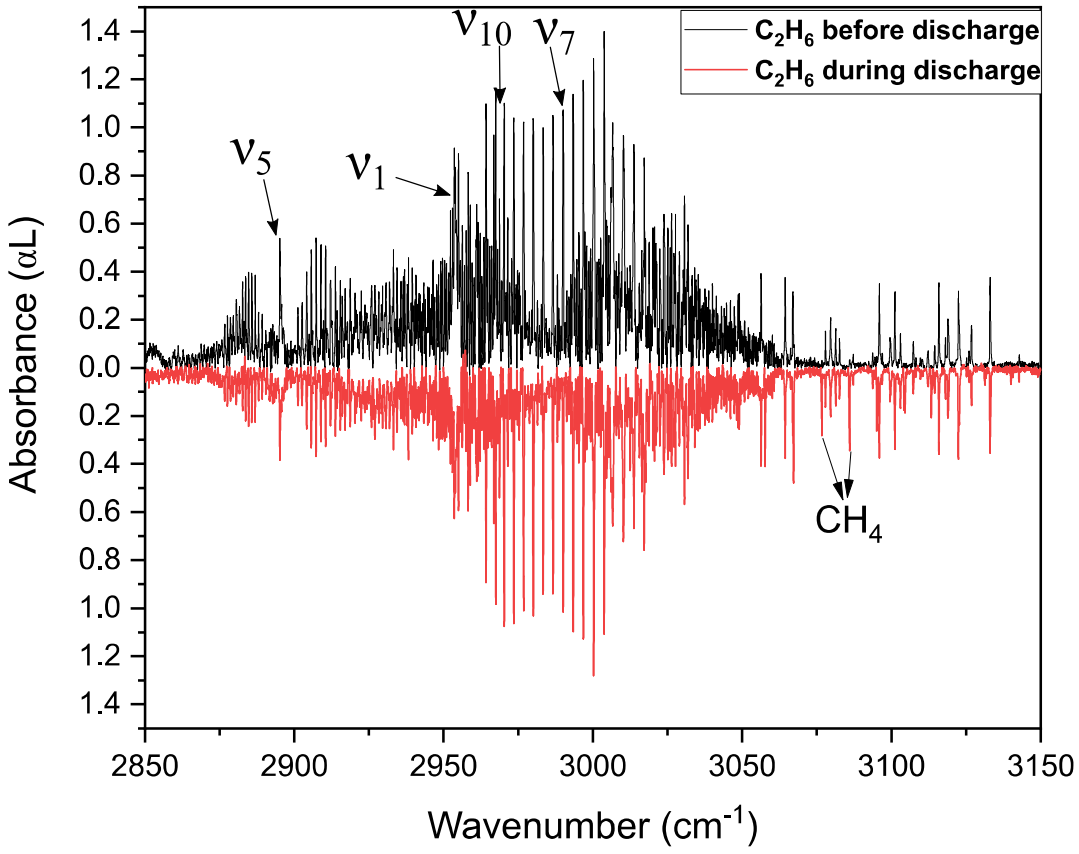

Figure 8. Absorption spectra of 33% C_2H_6 diluted in He, at 25 mbar before (in black, 700 averages) and during (in red, 700 averages, inverted for clarity) the discharge.

Preprints (www.preprints.org) | NOT PEER-REVIEWED | Posted: 17 September 2020 doi:10.20944/preprints202009.0397.v1

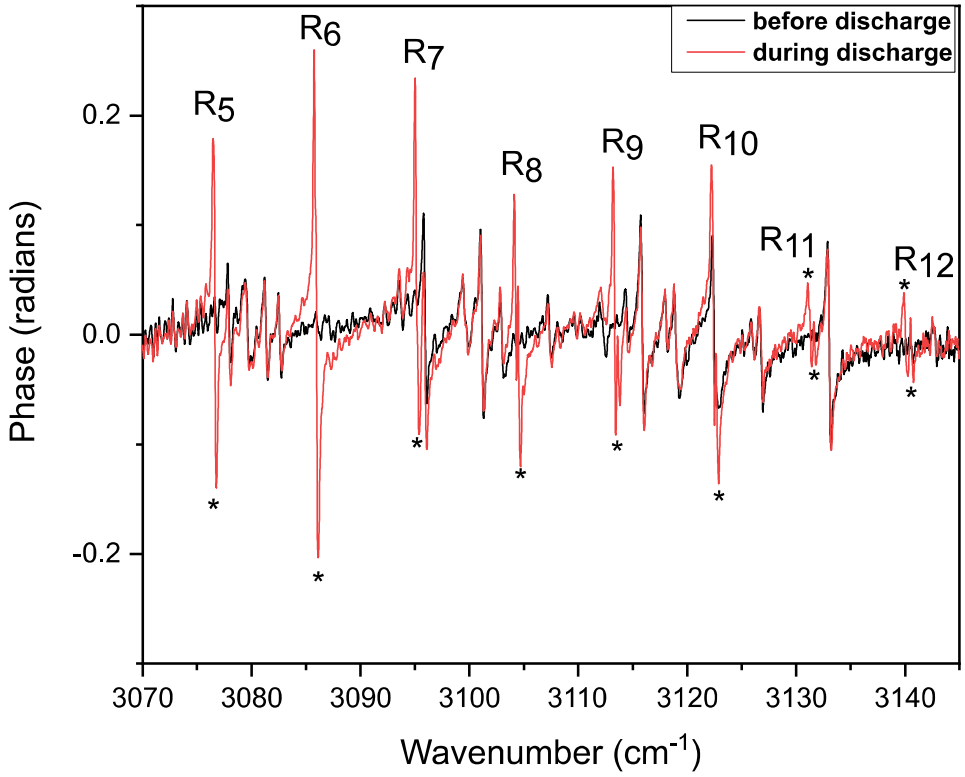

Figure 9. Part of the dispersion (phase) spectrum recorded before (in black, 700 averages) and during the discharge (in red, 700 averages) of 33% C_2H_6 diluted in He, at 25 mbar. Methane dispersion features appearing during the discharge are indicated by "*".

To observe dissociation of ethane and formation of methane during a DC static discharge plasma with different power levels, we measured the absorbance and phase changes of the gas sample while increasing the current density passing through the discharge tube from 0 mA/mm² (no discharge) to 2.12 mA/mm² (at ~10 kV). Figure 10 shows the absorption spectra of the gas sample at different discharge current densities. In order to show clearly the methane formation, we show only a small wavenumber range (3080-3130 cm^{-1}) of the total wavelength coverage (2850-3150 cm^{-1}). The increase in the strength of methane absorption features by increasing the discharge current density indicates ethane dissociation and the subsequent recombination of radicals forming methane.

Preprints (www.preprints.org) | NOT PEER-REVIEWED | Posted: 17 September 2020 doi:10.20944/preprints202009.0397.v1

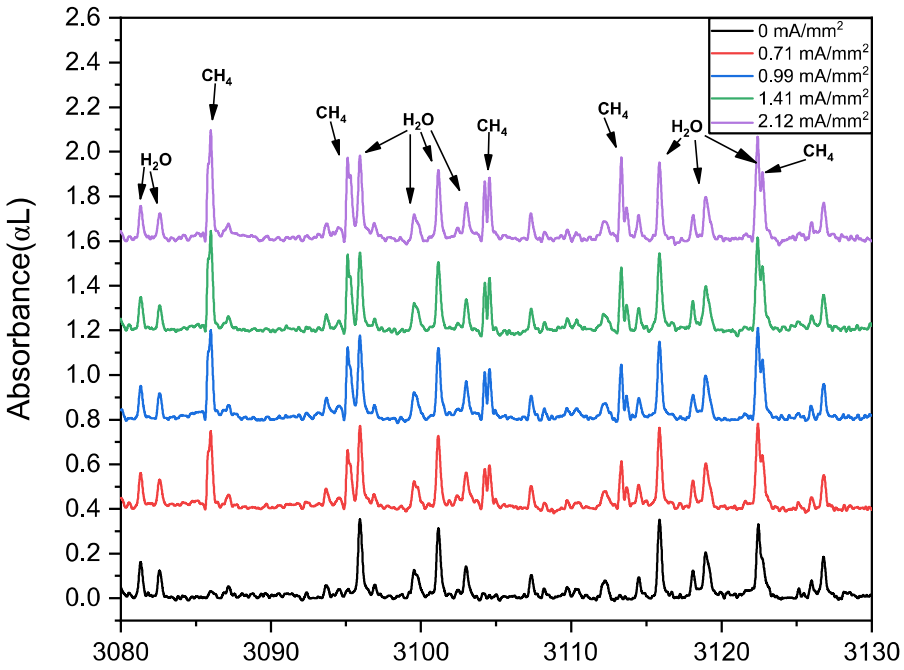

Figure 10. Absorption spectra of 33% C_2H_6 diluted in He at 25 mbar at different discharge current densities, demonstrating the generation of methane. For clarity, the spectra for different current densities are represented at different vertical offsets.

Figure 11 demonstrates the intensities of two methane and ethane absorption lines in terms of the discharge current density. The methane absorption features increase, while ethane absorption features decrease as expected. The same trends can be seen in the phase spectra in Figure 12.

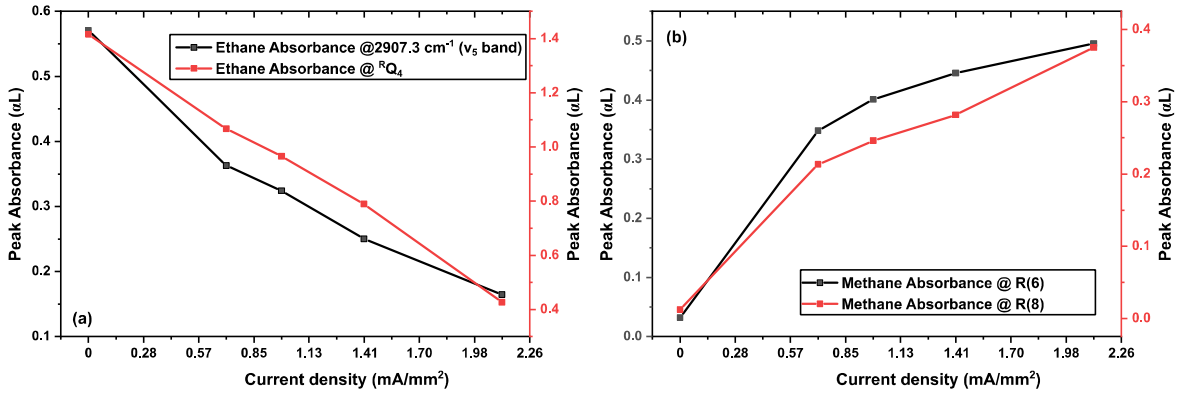

Figure 11. Change in methane and ethane peak absorbances in a 33% C_2H_6 diluted in He gas sample at 25 mbar upon increasing discharge current. Multiple peaks of both molecules are plotted to show the consistency over the vibrational bands.

Preprints (www.preprints.org) | NOT PEER-REVIEWED | Posted: 17 September 2020 doi:10.20944/preprints202009.0397.v1

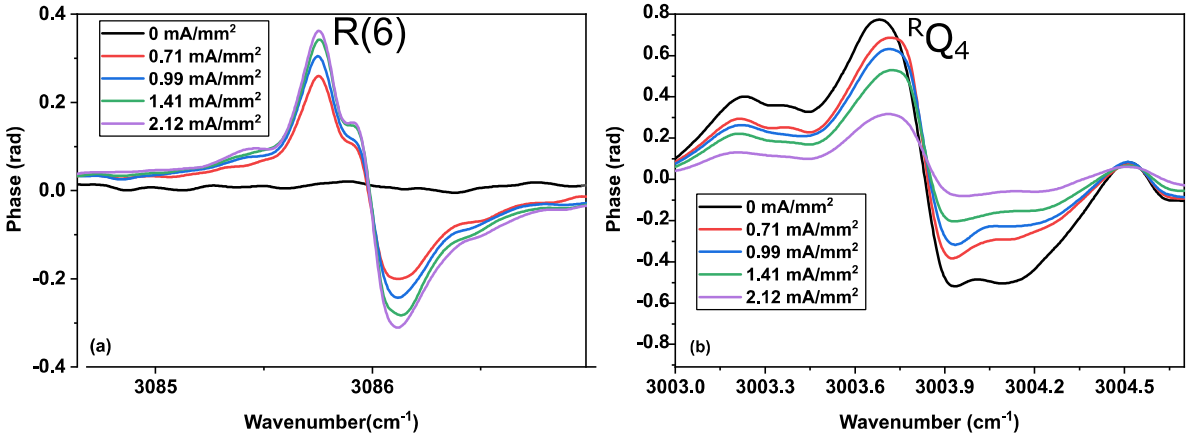

Figure 12. (a) Dispersion (phase) spectra of an R(6) line of methane ν_3 band, produced during the discharge of a gas sample (33% C_2H_6 diluted in He, at 25 mbar) and **(b)** dispersion of an $^RQ_4$ line of ethane ν_7 band, upon increasing the discharge current density.

3.4. Time Resolved Dynamics at Microseconds Timescale

The rapid acquisition time in dual-comb spectroscopy enables us to monitor the fast dynamical process, while changing the discharge at a microseconds time scale. Here, we study the absorption and phase transient dynamics of methane and ethane, during a pulsed discharge in a gas mixture of 40% CH_4 in He (25 mbar, flow rate 1.5 Nl/h). A square wave modulation at 265 Hz and 10% duty cycle, was applied to the discharge current (off: 0 mA and on: 0.99 mA/mm^2, voltage 10 KV). As mentioned earlier, the signal generator frequency was equal to, and synchronized (phase locked) with the difference repetition rate of the two comb sources (Δf_{rep}). Since the data acquisition should be synchronized as well, we used the second channel of the signal generator to trigger the DAQ card. This second channel was synchronized with the first channel and was manually delayed with respect to the first one. Therefore, time-resolved measurements could be performed at different triggering times after the discharge process in a step-scan manner. At each time step (minimum step size of 20 μs), the interferograms were acquired for 3.3 seconds (~900 averages), which included a single-shot acquisition time of 240 μs per interferogram. The interferograms were measured with a step size of 20 μs close to the on/off switching events of the discharge. We increased the step size further away from the switching events, where the discharge processes settles to semi-equilibrium values [30].

Figure 13 shows broadband time resolved absorption and dispersion dynamics of methane and ethane at specific times, relative to the rising and falling edge of the discharge pulses. Line by line analysis in the wavenumber region of 2971-3003 cm^{-1}, shows that during the on-time of the discharge, neutral gas species get excited and dissociate into radicals, thereby showing the decrease in the concentration of both methane and ethane (at the ground state), as indicated by the magnitude of absorption and dispersion signals in Figure 13 (a) and (b) respectively. However during the off-time of the discharge pulses, the produced radicals, will recombine to form C_2H_6 and CH_4, showing an increase in the absorption and dispersion signals in Figure 13 (c) and (d) respectively. These broadband time profiles of ro-vibrational transitions of both methane and ethane are interesting as they show a similar dynamics with respect to the dissociation and recombination of gas species given in [30].

Preprints (www.preprints.org) | NOT PEER-REVIEWED | Posted: 17 September 2020 doi:10.20944/preprints202009.0397.v1

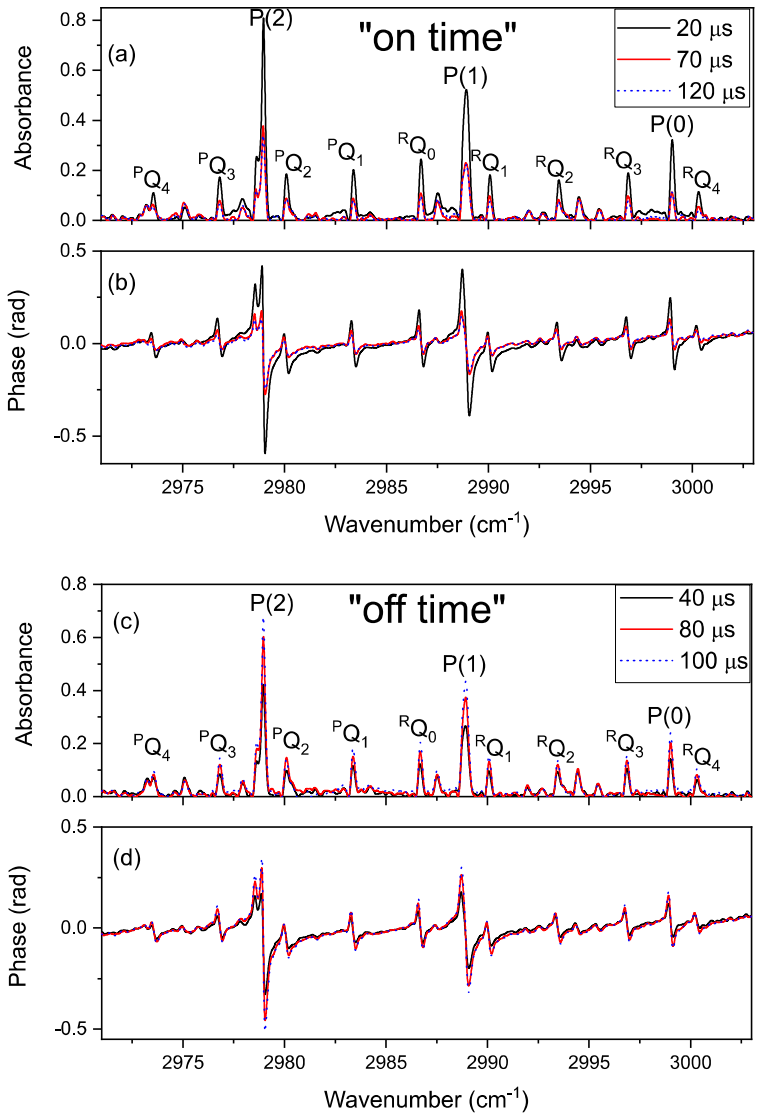

Figure 13. (a) and (b) Time-resolved absorption/dispersion spectra of CH_4 (P(2), P(1) and P(0) lines) and C_2H_6 (other lines) at 20, 70 and 120 µs after switching the discharge on. They show a decrease in concentration of both gas species. **(c) and (d)** Time-resolved absorption/dispersion spectra at the same wavenumber span measured in 40, 80, 100 µs after switching the discharge off, showing an increase in the concentrations, indicating the formation of CH_4 and C_2H_6, via recombination processes of hydrocarbon radicals.

In order to show, the complete time-profile of dissociation and formation of methane and ethane during an entire period of the discharge modulation we measured the magnitude of absorbance and dispersion peaks of two different methane (P(1) and P(6)) and ethane ($^{R}Q_0$ and $^{P}Q_1$) lines, as shown in Figure 14. In all cases, the spectra show that the methane/ethane population decreases rapidly (~ 50 µs), after the discharge has been switched on, indicating dissociation and the formation of radicals, ions and transient excited states of the molecules. After the discharge has been switched off, the radicals recombine again forming methane, and ethane. The recombination process can be seen by the increase in the absorbance/phase intensities. However in contrast to dissociation, the recombination process shows a slower exponential rise (~500 µs). These time resolved dynamics of abrupt decrease and slower increase in concentration show a similar time scale trends given in [30]

Preprints (www.preprints.org) | NOT PEER-REVIEWED | Posted: 17 September 2020 doi:10.20944/preprints202009.0397.v1

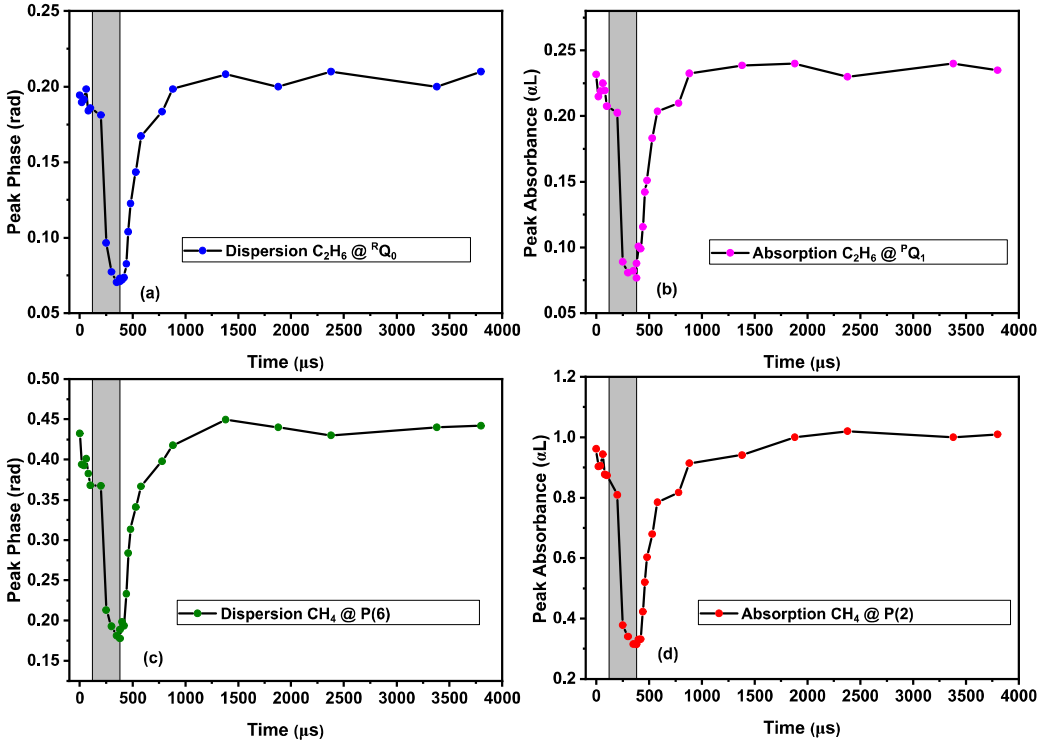

Figure 14. Time-resolved monitoring of the absorption/dispersion features of C_2H_6 in (a) and (b), and CH_4 in (c) and (d) at microseconds timescale. The discharge "on" time is shown with gray rectangles.

4. Conclusion

Obtaining broadband time-resolved dispersion spectra is difficult using a classical FTS. Here, we demonstrate for the first time capability of time-resolved mid-infrared DCS simultaneously recording absorption and dispersion spectra in a discharge plasma. The simultaneous recording enables to obtain directly the broadband complex refractive index of the gas sample.

DCS can also be used to measure the free induction decay of samples under study in the dual-comb interferogram, since we obtain an asymmetric (one sided) interferogram, which has a central burst in the middle and free induction decay of the sample mostly on the tail of the interferogram [56]. A truncated interferogram of 70 μs showing this phenomenon is demonstrated in Appendix Figure A2, for both methane and ethane samples.

Using other PPLN-poling periods of the crystal in the OPO, the wavelength range can be extended from 2200 to 4000 cm^{-1}, enabling the study of a wide range of molecules, ions and radicals, which have fundamental ro-vibrational transitions in that wavelength region. For instance, the CH_4/N_2 mixture will also produce HCN and NH_3 in a discharge. Future studies are planned to perform broadband time-resolved spectroscopy for other interesting species in a discharge.

There are certain limitations associated with our DCS, which are primarily because of the free running f_{ceo} of the frequency combs. In order to remove the f_{ceo} fluctuations, we used a reference absorption cell for absolute frequency calibration by using a single and well-known absorption line and consequently averaging the spectra. This whole arrangement makes a stringent requirement of perfectly balanced beam paths and post processing algorithm, to align the spectra before averaging. Therefore, this configuration is more practical for short path lengths in light-matter interaction. Increasing the interaction length using a multipass cell or an enhancement resonant cavity around the discharge can still be possible in this configuration. However, a second and similar reference multipass cell or enhancement cavity is required to achieve balanced beam paths.

Author Contributions: Conceptualization, A.K., M.A.A. and F.J.M.H.; methodology, A.K., and M.A.A. ; software, M.A.A., and A.K.; validation, M.A.A., A.K. and F.J.M.H.; formal analysis, M.A.A.; investigation, A.K., and F.J.M.H.; data curation, M.A.A., and L.V.D.; writing—original draft preparation, M.A.A., and L.V.D.;

Preprints (www.preprints.org) | NOT PEER-REVIEWED | Posted: 17 September 2020 doi:10.20944/preprints202009.0397.v1

writing—review and editing, A.K., F.J.M.H, K.E.J., M.N., and M.A.A.; visualization, M.A.A., and L.V.D.; supervision, F.J.M.H., and A.K.; project administration, F.J.M.H.; funding acquisition, F.J.M.H.

Funding: This research was funded by Dutch Technology Foundation (NWO), grant number 11830 and EU H2020-ICT29 (FLAIR project) grant number 732968.

Acknowledgments: Author(s) like to thank Yuwei Jin and Julien Mandon for their comments and previous work on mid-infrared dispersion spectroscopy in our group.

Conflicts of Interest: The authors declare no conflict of interest. The funders had no role in the design of the study; in the collection, analyses, or interpretation of data; in the writing of the manuscript, or in the decision to publish the results.

Appendix A

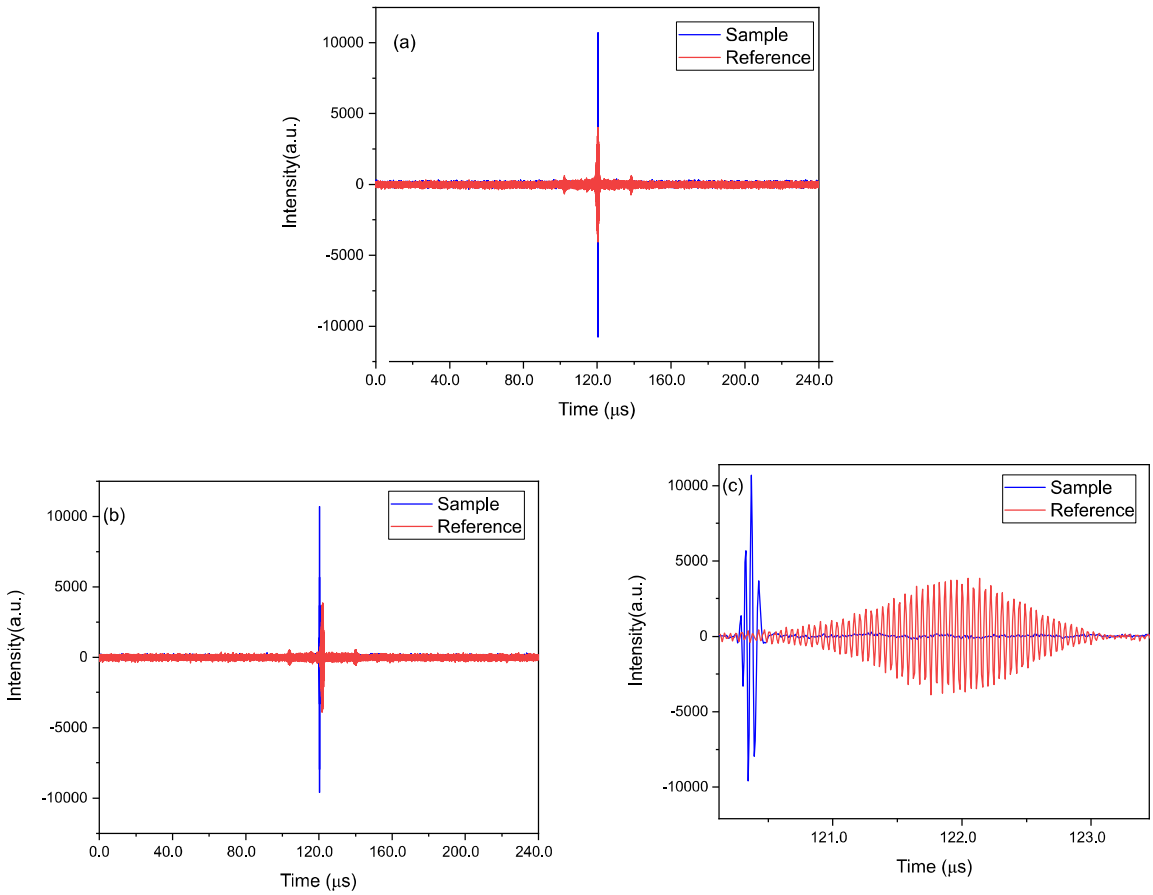

Figure A1. (a) Measured sample and reference interferograms with perfectly balanced beam paths. (b), (c) The influence of 3 mm CaF_2 window in the path of one frequency comb beam before the beam splitter, causing a shift in the sample interferogram in time domain with respect to the reference interferogram.

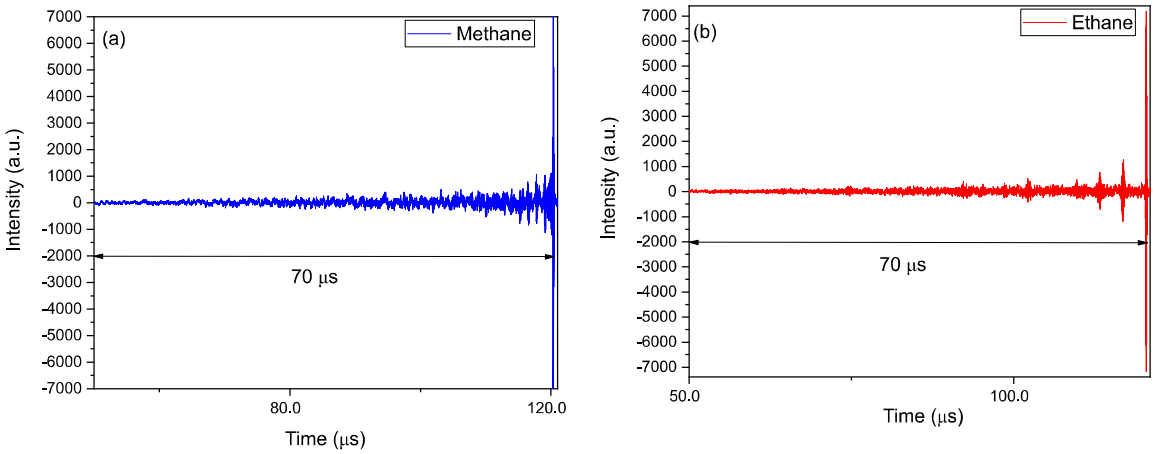

Figure A2. Truncated sample interferograms from methane in (a) and ethane (b) representing their optical free induction decay (FID).

References

1. Snoeckx, R.; Setareh, M.; Aerts, R.; Simon, P.; Maghari, A.; Bogaerts, A., Influence of N_2 concentration in a CH_4/N_2 dielectric barrier discharge used for CH_4 conversion into H_2. *International Journal of Hydrogen Energy* **2013,** 38, (36), 16098-16120, doi: https://doi.org/10.1016/j.ijhydene.2013.09.136.
2. Xu, C.; Tu, X., Plasma-assisted methane conversion in an atmospheric pressure dielectric barrier discharge reactor. *Journal of Energy Chemistry* **2013,** 22, (3), 420-425, doi: https://doi.org/10.1016/S2095-4956(13)60055-8.
3. Vastola, F. J.; Wightman, J. P., The rearrangement of acetylene, benzene, ethane, ethylene, methane and naphthalene in a microwave discharge. *Journal of Applied Chemistry* **1964,** 14, (2), 69-73, doi: 10.1002/jctb.5010140203.
4. Li, X.-S.; Zhu, A.-M.; Wang, K.-J.; Xu, Y.; Song, Z.-M., Methane conversion to C_2 hydrocarbons and hydrogen in atmospheric non-thermal plasmas generated by different electric discharge techniques. *Catalysis Today* **2004,** 98, (4), 617-624, doi: https://doi.org/10.1016/j.cattod.2004.09.048.
5. Gautier, T.; Carrasco, N.; Stefanovic, I.; Sikimic, B.; Cernogora, G.; Winter, J., Methane Conversion in a N_2-CH_4 Radiofrequency Discharge. *Plasma Processes and Polymers* **2014,** 11, (5), 472-481, doi: 10.1002/ppap.201300158.
6. Majumdar, A.; Behnke, J. F.; Hippler, R.; Matyash, K.; Schneider, R., Chemical Reaction Studies in CH_4/Ar and CH_4/N_2 Gas Mixtures of a Dielectric Barrier Discharge. *The Journal of Physical Chemistry A* **2005,** 109, (41), 9371-9377, doi: 10.1021/jp053588a.
7. Cheesman, A.; Smith, J. A.; Ashfold, M. N. R.; Langford, N.; Wright, S.; Duxbury, G., Application of a Quantum Cascade Laser for Time-Resolved, in Situ Probing of CH_4/H_2 and C_2H_2/H_2 Gas Mixtures during Microwave Plasma Enhanced Chemical Vapor Deposition of Diamond. *The Journal of Physical Chemistry A* **2006,** 110, (8), 2821-2828, doi: 10.1021/jp056622u.
8. Zhao, G.-B.; John, S.; Zhang, J.-J.; Wang, L.; Muknahallipatna, S.; Hamann, J. C.; Ackerman, J. F.; Argyle, M. D.; Plumb, O. A., Methane conversion in pulsed corona discharge reactors. *Chemical Engineering Journal* **2006,** 125, (2), 67-79, doi: https://doi.org/10.1016/j.cej.2006.08.008.
9. Scapinello, M.; Delikonstantis, E.; Stefanidis, G. D., The panorama of plasma-assisted non-oxidative methane reforming. *Chemical Engineering and Processing: Process Intensification* **2017,** 117, 120-140, doi: https://doi.org/10.1016/j.cep.2017.03.024.
10. Fujii, T.; Syouji, K., Mass spectrometric studies of the neutral and ionic products in a methane/oxygen microwave discharge plasma. *The Journal of Physical Chemistry* **1993,** 97, (44), 11380-11384, doi: 10.1021/j100146a007.
11. Burlacov, I.; Hamann, S.; Spies, H. J.; Dalke, A.; Röpcke, J.; Biermann, H., A Novel Approach of Plasma Nitrocarburizing Using a Solid Carbon Active Screen – a Proof of Concept. *HTM Journal of Heat Treatment and Materials* **2017,** 72, (5), 254-259, doi: 10.3139/105.110334.
12. Hamann, S.; Burlacov, I.; Spies, H. J.; Biermann, H.; Röpcke, J., Spectroscopic investigations of plasma nitriding processes: A comparative study using steel and carbon as active screen materials. *Journal of Applied Physics* **2017,** 121, (15), 153301, doi: 10.1063/1.4980039.

13. Cunge, G.; Vempaire, D.; Touzeau, M.; Sadeghi, N., Broadband and time-resolved absorption spectroscopy with light emitting diodes: Application to etching plasma monitoring. *Applied Physics Letters* **2007,** 91, (23), 231503, doi: 10.1063/1.2822448.
14. Bergevin, J.; Wu, T.-H.; Yeak, J.; Brumfield, B. E.; Harilal, S. S.; Phillips, M. C.; Jones, R. J., Dual-comb spectroscopy of laser-induced plasmas. *Nature Communications* **2018,** 9, (1), 1273, doi: 10.1038/s41467-018-03703-0.
15. Cunge, G.; Fouchier, M.; Brihoum, M.; Bodart, P.; Touzeau, M.; Sadeghi, N., Vacuum UV broad-band absorption spectroscopy: a powerful diagnostic tool for reactive plasma monitoring. *Journal of Physics D: Applied Physics* **2011,** 44, (12), 122001, doi: 10.1088/0022-3727/44/12/122001.
16. Röpcke, J.; Lombardi, G.; Rousseau, A.; Davies, P., Application of mid-infrared tuneable diode laser absorption spectroscopy to plasma diagnostics: a review. *Plasma Sources Science and Technology* **2006,** 15, (4), S148.
17. Allah, Z. A.; Sawtell, D.; Kasyutich, V. L.; Martin, P. A., FTIR and QCL diagnostics of the decomposition of volatile organic compounds in an atmospheric pressure dielectric packed bed plasma reactor. *Journal of Physics: Conference Series* **2009,** 157, 012001, doi: 10.1088/1742-6596/157/1/012001.
18. Hempel, F.; Davies, P. B.; Loffhagen, D.; Mechold, L.; Röpcke, J., Diagnostic studies of H_2–Ar–N_2 microwave plasmas containing methane or methanol using tunable infrared diode laser absorption spectroscopy. *Plasma Sources Science and Technology* **2003,** 12, (4), S98-S110, doi: 10.1088/0963-0252/12/4/025.
19. Röpcke, J.; Revalde, G.; Osiac, M.; Li, K.; Meichsner, J., Tunable Diode Laser Absorption Studies of Hydrocarbons in RF Plasmas Containing Hexamethyldisiloxane. *Plasma Chemistry and Plasma Processing* **2002,** 22, (1), 137-157, doi: 10.1023/A:1012996700044.
20. Welzel, S.; Hempel, F.; Hübner, M.; Lang, N.; Davies, P. B.; Röpcke, J., Quantum Cascade Laser Absorption Spectroscopy as a Plasma Diagnostic Tool: An Overview. *Sensors* **2010,** 10, (7), doi: 10.3390/s100706861.
21. Röpcke, J.; Davies, P. B.; Hamann, S.; Hannemann, M.; Lang, N.; Van Helden, J.-P. H., Applying Quantum Cascade Laser Spectroscopy in Plasma Diagnostics. *Photonics* **2016,** 3, (3), doi: 10.3390/photonics3030045.
22. Weichman, M. L.; Changala, P. B.; Ye, J.; Chen, Z.; Yan, M.; Picqué, N., Broadband molecular spectroscopy with optical frequency combs. *Journal of Molecular Spectroscopy* **2019,** 355, 66-78, doi: https://doi.org/10.1016/j.jms.2018.11.011.
23. Villares, G.; Hugi, A.; Blaser, S.; Faist, J., Dual-comb spectroscopy based on quantum-cascade-laser frequency combs. *Nature Communications* **2014,** 5, (1), 5192, doi: 10.1038/ncomms6192.
24. Schliesser, A.; Picqué, N.; Hänsch, T. W., Mid-infrared frequency combs. *Nature Photonics* **2012,** 6, (7), 440-449, doi: 10.1038/nphoton.2012.142.
25. Pinkowski, N. H.; Ding, Y.; Strand, C. L.; Hanson, R. K.; Horvath, R.; Geiser, M., Dual-comb spectroscopy for high-temperature reaction kinetics. *Measurement Science and Technology* **2020,** 31, (5), 055501, doi: 10.1088/1361-6501/ab6ecc.
26. Zhang, G.; Horvath, R.; Liu, D.; Geiser, M.; Farooq, A., QCL-Based Dual-Comb Spectrometer for Multi-Species Measurements at High Temperatures and High Pressures. *Sensors* **2020,** 20, (12), doi: 10.3390/s20123602.
27. Hoghooghi, N.; Cole, R. K.; Rieker, G. B., 11-{\mu}s Time-resolved, Continuous Dual-Comb Spectroscopy with Spectrally Filtered Mode-locked Frequency Combs. In *arXiv e-prints*, 2020; p arXiv:2005.13050.
28. Klocke, J. L.; Mangold, M.; Allmendinger, P.; Hugi, A.; Geiser, M.; Jouy, P.; Faist, J.; Kottke, T., Single-Shot Sub-microsecond Mid-infrared Spectroscopy on Protein Reactions with Quantum Cascade Laser Frequency Combs. *Analytical Chemistry* **2018,** 90, (17), 10494-10500, doi: 10.1021/acs.analchem.8b02531.
29. Luo, P.-L.; Horng, E.-C., Simultaneous determination of transient free radicals and reaction kinetics by high-resolution time-resolved dual-comb spectroscopy. *Communications Chemistry* **2020,** 3, (1), 95, doi: 10.1038/s42004-020-00353-6.
30. Abbas, M. A.; Pan, Q.; Mandon, J.; Cristescu, S. M.; Harren, F. J. M.; Khodabakhsh, A., Time-resolved mid-infrared dual-comb spectroscopy. *Scientific Reports* **2019,** 9, (1), 17247, doi: 10.1038/s41598-019-53825-8.
31. Birch, J. R., Dispersive Fourier transform spectroscopy. *Microchimica Acta* **1987,** 93, (1), 105-122, doi: 10.1007/BF01201686.
32. BELL, E., E., THE USE OF ASYMMETRIC INTERFEROGRAMS IN TRANSMITTANCE MEASUREMENTS. *J. Phys. Colloques* **1967,** 28, (C2), C2-18-C2-25.

33. Jin, Y.; Cristescu, S. M.; Harren, F. J. M.; Mandon, J., Two-crystal mid-infrared optical parametric oscillator for absorption and dispersion dual-comb spectroscopy. *Opt. Lett.* **2014,** 39, (11), 3270-3273, doi: 10.1364/OL.39.003270.
34. Gianella, M.; Nataraj, A.; Tuzson, B.; Jouy, P.; Kapsalidis, F.; Beck, M.; Mangold, M.; Hugi, A.; Faist, J.; Emmenegger, L., High-resolution and gapless dual comb spectroscopy with current-tuned quantum cascade lasers. *Opt. Express* **2020,** 28, (5), 6197-6208, doi: 10.1364/OE.379790.
35. Giorgetta, F. R.; Rieker, G. B.; Baumann, E.; Swann, W. C.; Sinclair, L. C.; Kofler, J.; Coddington, I.; Newbury, N. R., Broadband Phase Spectroscopy over Turbulent Air Paths. *Physical Review Letters* **2015,** 115, (10), 103901, doi: 10.1103/PhysRevLett.115.103901.
36. Coddington, I.; Swann, W. C.; Newbury, N. R., Coherent Multiheterodyne Spectroscopy Using Stabilized Optical Frequency Combs. *Physical Review Letters* **2008,** 100, (1), 013902, doi: 10.1103/PhysRevLett.100.013902.
37. Rutkowski, L.; Johansson, A. C.; Zhao, G.; Hausmaninger, T.; Khodabakhsh, A.; Axner, O.; Foltynowicz, A., Sensitive and broadband measurement of dispersion in a cavity using a Fourier transform spectrometer with kHz resolution. *Opt. Express* **2017,** 25, (18), 21711-21718, doi: 10.1364/OE.25.021711.
38. Johansson, A. C.; Rutkowski, L.; Filipsson, A.; Hausmaninger, T.; Zhao, G.; Axner, O.; Foltynowicz, A., Broadband calibration-free cavity-enhanced complex refractive index spectroscopy using a frequency comb. *Opt. Express* **2018,** 26, (16), 20633-20648, doi: 10.1364/OE.26.020633.
39. Weeks, R. R. D.; Zhang, Y.; Lecaplain, C.; Yeak, J.; Harilal, S. S.; Phillips, M. C.; Jones, R. J. In *Time-Resolved Dual Frequency Comb Phase Spectroscopy of Laser-Induced Plasmas*, Conference on Lasers and Electro-Optics, San Jose, California, 2019/05/05, 2019; Optical Society of America: San Jose, California, 2019; p JTh2A.106.
40. Cygan, A.; Wcislo, P.; Wojtewicz, S.; Maslowski, P.; Hodges, J. T.; Ciurylo, R.; Lisak, D., One-dimensional frequency-based spectroscopy. *Opt. Express* **2015,** 23, (11), 14472-14486, doi: 10.1364/oe.23.014472.
41. Nikodem, M.; Wysocki, G., Molecular dispersion spectroscopy – new capabilities in laser chemical sensing. *Annals of the New York Academy of Sciences* **2012,** 1260, (1), 101-111, doi: 10.1111/j.1749-6632.2012.06660.x.
42. Bjorklund, G. C., Frequency-modulation spectroscopy: a new method for measuring weak absorptions and dispersions. *Opt. Lett.* **1980,** 5, (1), 15-17, doi: 10.1364/OL.5.000015.
43. Ye, J.; Ma, L.-S.; Hall, J. L., Ultrasensitive detections in atomic and molecular physics: demonstration in molecular overtone spectroscopy. *J. Opt. Soc. Am. B* **1998,** 15, (1), 6-15, doi: 10.1364/JOSAB.15.000006.
44. Foltynowicz, A.; Schmidt, F. M.; Ma, W.; Axner, O., Noise-immune cavity-enhanced optical heterodyne molecular spectroscopy: Current status and future potential. *Applied Physics B* **2008,** 92, (3), 313, doi: 10.1007/s00340-008-3126-z.
45. Martín-Mateos, P.; Hayden, J.; Acedo, P.; Lendl, B., Heterodyne Phase-Sensitive Dispersion Spectroscopy in the Mid-Infrared with a Quantum Cascade Laser. *Analytical Chemistry* **2017,** 89, (11), 5916-5922, doi: 10.1021/acs.analchem.7b00303.
46. Wysocki, G.; Weidmann, D., Molecular dispersion spectroscopy for chemical sensing using chirped mid-infrared quantum cascade laser. *Opt. Express* **2010,** 18, (25), 26123-26140, doi: 10.1364/OE.18.026123.
47. Lewicki, R.; Doty, J. H.; Curl, R. F.; Tittel, F. K.; Wysocki, G., Ultrasensitive detection of nitric oxide at 5.33 μm by using external cavity quantum cascade laser-based Faraday rotation spectroscopy. *Proceedings of the National Academy of Sciences* **2009,** 106, (31), 12587-12592, doi: 10.1073/pnas.0906291106.
48. Mandon, J.; Guelachvili, G.; Picqué, N., Fourier transform spectroscopy with a laser frequency comb. *Nature Photonics* **2009,** 3, (2), 99-102, doi: 10.1038/nphoton.2008.293.
49. Gohle, C.; Stein, B.; Schliesser, A.; Udem, T.; Hänsch, T. W., Frequency Comb Vernier Spectroscopy for Broadband, High-Resolution, High-Sensitivity Absorption and Dispersion Spectra. *Physical Review Letters* **2007,** 99, (26), 263902, doi: 10.1103/PhysRevLett.99.263902.
50. Abbas, M. A.; Khodabakhsh, A.; Pan, Q.; Mandon, J.; Cristescu, S. M.; Harren, F. J. M., Mid-infrared dual-comb spectroscopy with absolute frequency calibration using a passive optical reference. *Opt. Express* **2019,** 27, (14), 19282-19291, doi: 10.1364/OE.27.019282.
51. Alrefae, M.; Es-sebbar, E.-t.; Farooq, A., Absorption cross-section measurements of methane, ethane, ethylene and methanol at high temperatures. *Journal of Molecular Spectroscopy* **2014,** 303, 8-14, doi: https://doi.org/10.1016/j.jms.2014.06.007.
52. Sahlberg, A.-L.; Zhou, J.; Aldén, M.; Li, Z., Investigation of ro-vibrational spectra of small hydrocarbons at elevated temperatures using infrared degenerate four-wave mixing. *Journal of Raman Spectroscopy* **2016,** 47, (9), 1130-1139, doi: 10.1002/jrs.4862.

53. Sanchez-Gonzalez, R.; Kim, Y.; Rosocha, L. A.; Abbate, S., Methane and Ethane Decomposition in an Atmospheric-Pressure Plasma Jet. *IEEE Transactions on Plasma Science* **2007,** 35, (6), 1669-1676, doi: 10.1109/TPS.2007.910743.

54. De Bie, C.; Martens, T.; van Dijk, J.; Paulussen, S.; Verheyde, B.; Corthals, S.; Bogaerts, A., Dielectric barrier discharges used for the conversion of greenhouse gases: modeling the plasma chemistry by fluid simulations. *Plasma Sources Science and Technology* **2011,** 20, (2), 024008, doi: 10.1088/0963-0252/20/2/024008.

55. Gordon, I. E.; Rothman, L. S.; Hill, C.; Kochanov, R. V.; Tan, Y.; Bernath, P. F.; Birk, M.; Boudon, V.; Campargue, A.; Chance, K. V.; Drouin, B. J.; Flaud, J. M.; Gamache, R. R.; Hodges, J. T.; Jacquemart, D.; Perevalov, V. I.; Perrin, A.; Shine, K. P.; Smith, M. A. H.; Tennyson, J.; Toon, G. C.; Tran, H.; Tyuterev, V. G.; Barbe, A.; Császár, A. G.; Devi, V. M.; Furtenbacher, T.; Harrison, J. J.; Hartmann, J. M.; Jolly, A.; Johnson, T. J.; Karman, T.; Kleiner, I.; Kyuberis, A. A.; Loos, J.; Lyulin, O. M.; Massie, S. T.; Mikhailenko, S. N.; Moazzen-Ahmadi, N.; Müller, H. S. P.; Naumenko, O. V.; Nikitin, A. V.; Polyansky, O. L.; Rey, M.; Rotger, M.; Sharpe, S. W.; Sung, K.; Starikova, E.; Tashkun, S. A.; Auwera, J. V.; Wagner, G.; Wilzewski, J.; Wcisło, P.; Yu, S.; Zak, E. J., The HITRAN2016 molecular spectroscopic database. *Journal of Quantitative Spectroscopy and Radiative Transfer* **2017,** 203, 3-69, doi: https://doi.org/10.1016/j.jqsrt.2017.06.038.

56. Coddington, I.; Swann, W. C.; Newbury, N. R., Time-domain spectroscopy of molecular free-induction decay in the infrared. *Opt. Lett.* **2010,** 35, (9), 1395-1397, doi: 10.1364/OL.35.001395.